

## A thin viscous sheet model for continental deformation

Philip England<sup>\*</sup> and Dan McKenzie *Department of Earth Sciences,  
University of Cambridge, Bullard Laboratories, Madingley Rise, Madingley Road,  
Cambridge CB3 0EZ*

Received 1981 September 22; in original form 1980 December 17

**Summary.** For the purposes of describing its large-scale and long-term deformation, the continental lithosphere is regarded as a continuum, obeying a Newtonian or a power law rheology. The flow of a thin sheet of power law material overlying an inviscid substrate is studied under the assumption that vertical gradients of the horizontal velocity are negligible. A numerical model is used to investigate the deformation of such a sheet under conditions approximating those of continent–continent collision. The material flows in response to forces applied to its boundaries (for example, the indenting of one continent by another) and to forces in its interior arising from gradients in crustal thickness. The horizontal divergence of the flow produces changes in the crustal thickness and hence a time-dependent form to the flow itself. For a given set of boundary conditions, the flow depends on the stress exponent in the power law rheology,  $n$ , and on the Argand number  $Ar$ , which is a measure of the ratio between the stress arising from crustal thickness contrasts and the stress required to deform the material at the ambient strain rates. When the effective viscosity of the medium is very high ( $Ar \rightarrow 0$ ), crustal thickness variations do not influence the flow. If the material is Newtonian ( $n = 1$ ), the deformation associated with an influx of material (approximating an indenter) is of much greater lateral dimension than the width of the indenter, whereas when material has a power law rheology ( $n = 3, 5$  are used), the deformation is confined to a region of lateral extent comparable to that of the indenter. As  $Ar$  increases, the forces arising from crustal thickness contrasts exert more influence on the flow, and the maximum crustal thickness that can be sustained by a given influx of material is related by a simple expression to the effective viscosity of the medium at the ambient strain rates. In the limit of a very weak medium ( $Ar > 10$ ) the lithosphere is unable to sustain appreciable crustal elevation contrasts. The results of these numerical experiments show that systems in which the effective viscosities are such that the maximum deviatoric stresses are between 1 kbar

<sup>\*</sup> Present address: Department of Geological Sciences, Harvard University, 20 Oxford Street, Cambridge, Massachusetts 02138, USA.

and 100 bar have crustal thickness distributions comparable to that in the India–Asia collision zone. In addition, these systems have the characteristic that the forces arising from crustal thickness contrasts are great enough to produce net extension in the region of thick crust in front of the influx boundary, perpendicular to the direction of influx, as well as lateral movement away from the region of thickest crust. Observations of contemporary tectonics in Asia show phenomena very similar to these, in the active east–west extension of Tibet and the eastward motion of eastern Tibet.

## 1 Introduction

Plate tectonic theory has been successful in explaining much of the present and past deformation of the Earth. Certainly its fundamental tenet – that the plates are essentially rigid bodies – describes well the behaviour of the oceanic regions; oceanic deformation occurs almost entirely within belts a few tens of kilometres wide that take up the differential movements between otherwise rigid plates. However, it has been recognized for several years that the deformation of the continents represents a significant departure from the principles of plate tectonics (McKenzie 1972, 1976; Molnar & Tapponnier 1975; Tapponnier & Molnar 1976). For example the zone of collision between India and Asia is more than 2000 km wide and that between Africa and Europe is up to 1000 km wide. In both these zones there are regions with crust of one and a half times to twice the normal continental thickness and, although some of the seismicity and deformation appears to occur in narrow linear zones, much of it is diffuse in nature and cannot adequately be accounted for in terms of the relative motion of the large plates, or even of a greater number of small plates.

One approach to the crustal deformation in continental convergence zones has been to treat the collision in terms of the deformation of a rigid-plastic medium by a rigid indenter (Molnar & Tapponnier 1975; Tapponnier & Molnar 1976, 1977). In this approach, a condition of plane horizontal strain is assumed, and the slip lines calculated from the imposed boundary conditions are taken to indicate the approximate orientations expected for large-scale strike-slip faulting in the collision zone. A measure of qualitative success has been attained in relating the slip lines obtained from this kind of modelling to the orientations of major faults in Asia, and in other less well constrained collision zones.

However, as recognized by Molnar & Tapponnier, there are limitations to this approach which make it hard to apply in a quantitative way to the processes of continental deformation. First, the slip lines calculated are only appropriate for the onset of yielding in the rigid-plastic medium and their orientations will change as deformation proceeds. Although it is possible in principle to calculate the finite deformation of a rigid-plastic medium, in practice it is laborious, except in the simple case where the geometry remains constant but the scale increases (e.g. indentation by a wedge). In the plastic/indenter approach, as in the present one, the problem addressed is of the finite deformation of a continuous medium – *slip lines are not faults* – thus the relation between an instantaneous slip line and a major strike-slip fault which may have accommodated hundreds of kilometres of movement is problematic.

Secondly, the assumption of plane horizontal strain breaks down in areas where the crust has been appreciably thickened or thinned, and regions such as this extend more than 1000 km north of the Himalayas. Ignoring strain in the vertical direction affects not only the *geometry* of the deformation: crustal elevation contrasts will exert forces within the deforming medium in addition to those directly imposed by the boundary conditions. As the former forces may be comparable with those estimated to be available to drive plate motion

(e.g. Richter & McKenzie 1978) they ought not to be neglected in the treatment of zones of continental convergence.

In this paper we present results of some numerical experiments on the deformation of Newtonian and non-Newtonian viscous materials in response to boundary conditions approximating those of continental collision. Our approach permits the calculation of the time-dependent deformation and stress field, and – by taking account of the vertical strain – gives the development in time of crustal thickness variations. It also permits the calculation of deformation fields for differing assumptions about the effective viscosity of the continental lithosphere. Comparison of the results of numerical experiments with the deformation in the India–Asia collision zone suggests that the forces arising from crustal thickness contrasts may play an important role in the deformation of the continents.

## 2 Model formulation

In formulating a model for continental deformation it is necessary to make several assumptions about the rheology appropriate to the large-scale deformation of the continents and about the manner in which this deformation takes place. These assumptions are discussed in Section 2.1 and the mathematical formulation to which they lead is presented in Section 2.2.

### 2.1 ASSUMPTIONS

We assume that the variation with depth of the horizontal components of velocity within the lithosphere is negligible. This assumption is valid for the case of a thin viscous sheet overlying an inviscid fluid, provided that gradients of crustal thickness are small; these conditions are satisfied in the present case, as the lithosphere is underlain by asthenosphere much weaker than itself, and gradients of crustal thickness are small (see Section 4). It follows from this assumption that the rate at which the lithosphere strains in response to a given stress – or conversely the stress required to maintain a given strain rate – will be governed by the rheology of the strongest portion of the lithosphere. This formulation ignores the role of faulting in lithospheric deformation – something that is inevitable in any continuum approach to the problem. We discuss in Sections 4 and 5 some of the problems of relating the brittle deformation of the upper layers to the deformation of the lithosphere as a whole.

There have been relatively few reliable determinations of the rheological properties of crustal rocks, but those that there are indicate that crustal rocks may be weaker than the upper mantle under the conditions of temperature, pressure and strain rate appropriate to continental collision (e.g. Tullis 1979; table 1). It should be emphasized that the relevant strength is that involved in strains of tens of per cent over tens of millions of years and thus that the brittle layer is not regarded as governing the strength of the lithosphere. The formulation that follows does not depend on the detailed rheology of the continental lithosphere, but on some vertical average of it (Appendix A); we regard the question of what level, or levels, within the lithosphere control its strength as an open one, but in relating the numerical experiments described here to the properties of the continental lithosphere we shall use the uppermost mantle as a *plausible example* of this layer, because the rheologies of olivine and of mantle rocks have been investigated more than those of crustal materials.

Laboratory determinations of the rheology of olivine and other minerals representative of the crust and upper mantle indicate that they deform by power law creep according to a law like

$$\dot{\epsilon} = C(\sigma_1 - \sigma_3)^n \exp\left(\frac{-Q}{R\theta}\right) \quad (1)$$

in the range of conditions likely to apply to the deformation of the continental lithosphere.  $C$  is a constant of the material,  $\sigma_1$  and  $\sigma_3$  are the greatest and least principal stresses,  $\theta$  is the absolute temperature,  $R$  is the gas constant and  $Q$  is the activation energy for the relevant deformation mechanism. There may also be a dependence of the strain rate on the lithostatic pressure, but this is much weaker than the temperature dependence and is neglected here. Application of the rheology of equation (1) to the deformation of the continental lithosphere under the assumption of negligible vertical gradients of horizontal velocity shows that equation (1) may be replaced by a relation of the form:

$$\dot{\epsilon} = B^{-n} (\sigma_1 - \sigma_3)^n \quad (2)$$

where  $B$  now averages throughout the lithosphere the temperature-dependent parts of equation (1) (see Appendix A).  $B$  is to some extent sensitive to the thermal gradient assumed but it is principally dependent on the ratio  $Q/\theta_M$  (equation 1), where  $\theta_M$  is the absolute temperature at the top of the upper mantle. This simplification still applies if the strength of the lower crust is comparable with that of the upper mantle (see Appendix A), provided that  $n$  does not change within the strongest portion of the lithosphere. The problem may now be formulated in terms of the deformation of an homogeneous power law material that is assumed to be isotropic and incompressible.

## 2.2 MATHEMATICAL FORMULATION

In describing the flow of rocks at geological strain rates we may neglect momentum terms and the Navier-Stokes equation reduces to

$$\frac{\partial p}{\partial x_i} = \frac{\partial \tau_{ij}}{\partial x_j} - \rho g a_i \quad (3)$$

where  $\mathbf{a} = (0, 0, 1)$ ,  $\tau_{ij}$  are elements of the deviatoric stress tensor and  $p$  is the pressure in the field. The usual convention of summation over repeated subscripts holds. A constitutive relation like equation (2) is usually generalized in the form:

$$\dot{\epsilon}_{ij} = B^{-n} T^{n-1} \tau_{ij}. \quad (4)$$

$T$  is the second invariant of the deviatoric stress tensor

$$T = (\tau_{kl} \tau_{kl})^{1/2} \quad (5)$$

and the strain rate tensor is defined by

$$\dot{\epsilon}_{ij} = \frac{1}{2} \left( \frac{\partial u_i}{\partial x_j} + \frac{\partial u_j}{\partial x_i} \right) \quad (6)$$

where  $u_i$  and  $u_j$  are components of velocity in the directions of orthogonal coordinates  $x_i, x_j$ . From equation (4) we have

$$\tau_{ij} = B \dot{E}^{(1/n-1)} \dot{\epsilon}_{ij} \quad (7)$$

where  $\dot{E}$  is the second invariant of the strain rate tensor (cf. equation 5). The independence of depth of the horizontal components of velocity gives us

$$\dot{\epsilon}_{xz} = \dot{\epsilon}_{zx} = \dot{\epsilon}_{yz} = \dot{\epsilon}_{zy} = 0 \quad (8)$$

and the incompressibility of the fluid requires that

$$\dot{\epsilon}_{zz} = -(\dot{\epsilon}_{xx} + \dot{\epsilon}_{yy}). \quad (9)$$

The second invariant of the strain rate tensor may now be expressed entirely in terms of spatial derivatives of the horizontal components of velocity:

$$\dot{E} = \sqrt{2(\dot{\epsilon}_{xx}^2 + \dot{\epsilon}_{yy}^2 + \dot{\epsilon}_{xy}^2 + \dot{\epsilon}_{xx}\dot{\epsilon}_{yy})}^{1/2}. \quad (10)$$

Integration of the vertical pressure gradient obtained from (3) yields  $p$ , and substitution of  $p$  and  $\tau_{ij}$  from (7) into (3) then gives

$$\frac{\partial \bar{p}}{\partial x_i} = B \dot{E}^{(1/n-1)} \frac{\partial \dot{\epsilon}_{ij}}{\partial x_j} + B(1/n-1) \frac{\partial \dot{E}}{\partial x_j} \dot{E}^{1/n-2} \dot{\epsilon}_{ij} \quad (11)$$

where it is now understood that  $i$  and  $j$  represent only the two horizontal coordinates, and the pressure,  $p$ , in equation (3) has been replaced by the average of the pressure over the whole depth,  $L$ , of the lithosphere

$$\bar{p} = \frac{1}{L} \int_0^L p dz. \quad (12)$$

If the crust is of thickness  $s$  and density  $\rho_m$  equation (12) gives

$$\bar{p} = \frac{g\rho_c s^2}{2L} (1 - \rho_c/\rho_m) + \frac{g\rho_m L}{2}. \quad (13)$$

Rearranging equation (11), and using equation (13), we obtain

$$\frac{1}{2} \partial_j (\partial_j u_i + \partial_i u_j) = \frac{g\rho_c s}{BL} (1 - \rho_c/\rho_m) \dot{E}^{(1-1/n)} \frac{\partial s}{\partial x_i} + (1-1/n) \dot{E}^{-1} \frac{\partial \dot{E}}{\partial x_j} \dot{\epsilon}_{ij}. \quad (14)$$

The natural non-dimensionalization is

$$(x', s') = (x, s)/L; \quad u' = u/u_0; \quad t' = tL/u_0 \quad (15)$$

where  $t$  is time (equation 18). Equation (15) may be written in the non-dimensional form (dropping primes):

$$\nabla^2 \mathbf{u} = -\nabla(\nabla \cdot \mathbf{u}) + 2(1-1/n) \dot{E}^{-1} \nabla \dot{E} \cdot \dot{\epsilon} + 2Ar \dot{E}^{(1-1/n)} s \nabla s \quad (16)$$

where all operators refer to horizontal derivatives only, and

$$Ar = \frac{g\rho_c(1 - \rho_c/\rho_m)L^{(1+1/n)}}{Bu_0^{1/n}}. \quad (17)$$

The time-dependence of  $s$  may be determined, once  $\mathbf{u}$  is known, from the continuity equation

$$\frac{\partial s}{\partial t} = -\nabla \cdot (s\mathbf{u}) \quad (18)$$

with the non-dimensionalization of equation (15).

Equations (16) and (18), together with an initial condition on  $s$ , and boundary conditions on  $\mathbf{u}$  and  $s$  completely specify the time and space dependence of the velocity field and the crustal thickness. Details of the numerical solution of these equations are given in Appendix B.

### 3 Results

The formulation of Section 2 leads to a simple parametrization in which the flow for a given set of boundary conditions depends only on two parameters directly related to the

constitutive relation assumed for the material. The first,  $n$ , defines the power law dependence of the strain rate on the stress, and the second,  $Ar$ , is linked to the effective viscosity of the medium.

### 3.1 PARAMETER RANGES

It seems likely from laboratory experiments on olivine and mantle-derived rocks, and from more general considerations of the deformation mechanisms of ceramics that, under the ambient conditions of temperature, pressure and strain rate, the deformation of the uppermost mantle is controlled by the movement of dislocations. This mode of deformation results in power law creep with a stress exponent that is inferred from laboratory experiments to be about 3 for Earth materials (e.g. Ashby & Verrall 1978; Goetze 1978). However, the extrapolation of laboratory data to geological strain rates is notoriously uncertain, and it is also possible that diffusional flow (Newtonian,  $n = 1$ ) or grain size-dependent flow (which could result in power law flows with stress exponents greater than 3) predominate in the uppermost mantle (Ashby & Verrall 1978; Goetze 1978).

We have used values of 1, 3 and 5 for  $n$ ; as will be seen below the principal modifications to the flow come in the transformation from  $n = 1$  to 3, and raising  $n$  higher does not produce qualitatively different results.

Application of laboratory data to geological conditions is also uncertain with regard to the constant of proportionality between strain and (stress) <sup>$n$</sup>  –  $B$  in equation (2) – because of the exponential dependence of  $B$  on temperature (equations 1 and A3) and because of the extrapolation over several orders of magnitude that is necessary to relate laboratory strain rate data to geological processes. This uncertainty is expressed in the present formulation in terms of an uncertainty in  $Ar$  in equation (16).

The physical significance of  $Ar$  may be seen by rewriting equation (17) as:

$$Ar = \frac{g\rho_c L(1 - \rho_c/\rho_m)}{B(u_0/L)^{1/n}} = \frac{P(L)}{\tau(\dot{\epsilon}_0)} \quad (19)$$

where  $P(L)$  is an estimate of the excess pressure arising from a crustal thickness contrast of order  $L$  and  $\tau(\dot{\epsilon}_0)$  is the stress required to deform the medium at a strain rate characteristic of the system:

$$\dot{\epsilon}_0 = u_0/L. \quad (20)$$

We propose the name Argand number for this measure of the tendency of the lithosphere to strain in response to the buoyancy forces generated by crustal thickness contrasts. If  $Ar$  is small – i.e. if the effective viscosity of the medium is large at the ambient strain rates – then the flow will be governed by the boundary conditions. At the other extreme, if  $Ar$  is very large, the forces arising from crustal thickness variations will be dominant and the effective viscosity of the medium will not be great enough to support appreciable elevation contrasts.

The greater uncertainty in these models is the effective viscosity of the continental lithosphere at geological strain rates, so it is desirable to investigate as large a part of the parameter range as possible; it is found that the range of 0–30 in Argand number encompasses the extremes outlined in the previous paragraph.

### 3.2 BOUNDARY CONDITIONS

The means of solution of equation (16) restrict the geometry of the models to a rectangle or a system of overlapping rectangles; for the calculations described here we have chosen the simplest geometry rather than proceeding immediately to more complex configurations.

The deforming continental lithosphere is taken to be rectangular with rigid boundaries — zero normal and tangential velocity — except over part of one boundary where material identical to that of interior flows in at a rate that is a function of position but not, in these instances, of time. This flow is symmetrical and normal to the boundary, and solutions are obtained in one-half of the rectangle with the axis of symmetry as a free boundary. In all the experiments described below the rectangle has dimensions  $64L$  by  $32L$  and so solutions are found in a square of side  $32L$ . In accordance with the velocity boundary conditions the crustal thickness has zero gradient normal to the edges; in the first set of experiments to be described below this condition is replaced by one of constant thickness on the influx boundary. The geometry of the models is illustrated in Fig. 1.

### 3.3 SCALING

In presenting the results of the numerical experiments we have used the values of parameters given below:

Table 1.

$L$	$= 100 \text{ km}$
$u_0$	$= 50 \text{ mm yr}^{-1}$
$g$	$= 9.8 \text{ m s}^{-2}$
$\rho_c$	$= 2.95 \text{ Mg m}^{-3}$
$\rho_m$	$= 3.3 \text{ Mg m}^{-3}$

Apart from variations in crustal thickness, two important points of comparison between the solutions described below and observations of the deformation of the continents are the magnitudes of the strain rates and the deviatoric stresses predicted by the numerical experiment.

The relation of the stresses and strain rates to their non-dimensional equivalents are:

$$\dot{\epsilon}_{ij} = u_0/L \dot{\epsilon}'_{ij} \quad (21a)$$

$$\tau_{ij} = B \dot{E}^{(1/n-1)} \dot{\epsilon}_{ij} = B(u_0/L)^{1/n} \dot{E}'^{(1/n-1)} \dot{\epsilon}'_{ij} \quad (21b)$$

$$\tau_{ij} = \frac{g \rho_c L (1 - \rho_c/\rho_m)}{Ar} \dot{E}'^{(1/n-1)} \dot{\epsilon}'_{ij} \quad (21c)$$

where the dimensionless variables are primed.

The solutions presented below are for fixed values of Argand number and  $n$ , and it is important to know to what extent the choices of values for the parameters in Table 1 influence the magnitudes of the strain rates and stresses calculated from the solutions. The dependence of the strain rates on the choices of  $u_0$  and  $L$  is clear from equation (21a), and it can be seen from equation (21c) that the stresses for fixed values of  $L$ ,  $Ar$  and  $n$  are independent of the magnitude of the velocity used to dimensionalize the solution. It can also be seen from equations (21c) and (16) that for fixed  $u_0$ ,  $Ar$  and  $n$ , the stresses are proportional to the value of  $L$ . These two results are to be expected from the formulation of Section 2.

### 3.4 MODELS WITH ZERO ARGAND NUMBER

When the Argand number is zero, the flow in the medium is independent of time, although the crustal thickness variations will develop provided that  $\nabla \cdot (\mathbf{su})$  is not everywhere zero. In this set of experiments, the velocity boundary conditions of Fig. 1 were applied with the

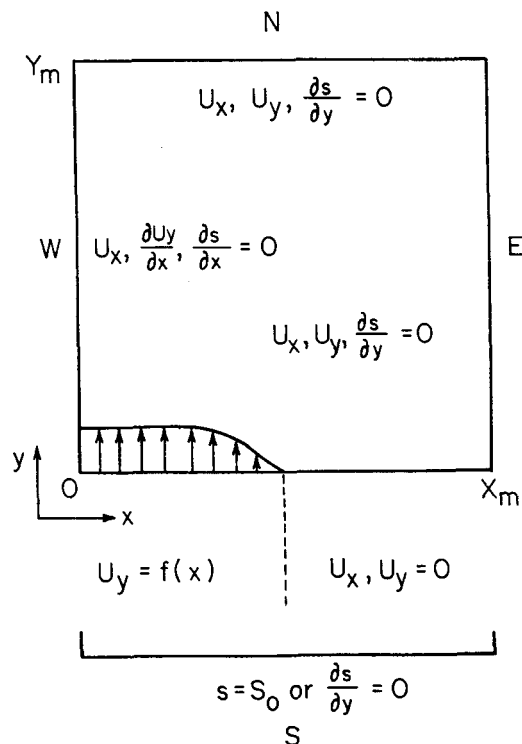


**Figure 1.** Geometry of the numerical models described in the text. Finite difference solutions to equation (16) are obtained on a mesh within the box (Appendix B), subject to the boundary conditions shown. In the models described in this paper  $X_m = Y_m = 32L$ . The function  $f(x)$  has the form:

$$f(x) = u_0; \quad 0 < x < X_m/4$$

$$f(x) = u_0 \cos^2 [\pi/2(4x/X_m - 1)] \quad X_m/4 \leq x \leq X_m/2.$$

For convenience of description, the points of the compass, as shown here, are used in the text when referring to different parts of the box.

initial condition that the crust be 35 km thick everywhere in the box; the boundary conditions on crustal thickness were those of Fig. 1, with the requirement that the crust on the  $x$ -axis was always 35 km thick.

Figs 2, 3 and 4 illustrate, for fluids with  $n = 1, 3$  and  $5$  respectively, the flow fields, the principal strain rates and the orientations and relative magnitudes of the principal deviatoric stresses arising from the velocity boundary conditions. Figs 5, 6 and 7 show the development with time of the crustal thickness, again for fluids with  $n = 1, 3, 5$ .

The velocity fields are plotted in Figs 2(d), 3(d) and 4(d) in the form of vectors having their origins at the positions of grid points in the finite difference mesh. The strain rate tensor corresponding to these fields is illustrated by contours of the isotropic strain rate (rate of extension or compression) and by crosses indicating the orientations and magnitudes of the principal shear strain rates (Figs 2a,c, 3a,c, 4a,c). Figs 2(b), 3(b) and 4(b) show the orientations and the relative magnitudes of the principal stresses in the medium. Note that when the Argand number is zero the effective viscosity of the system is undefined (equation 21c) and the stresses have arbitrary absolute magnitudes.



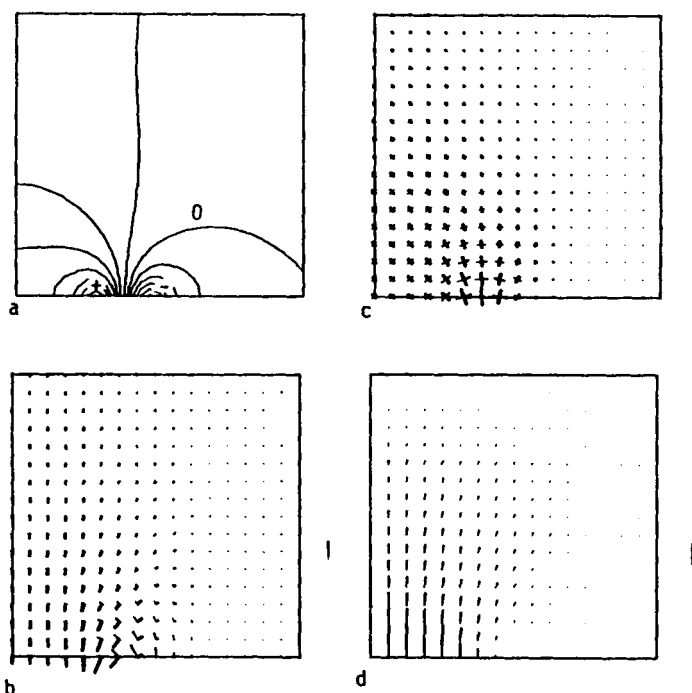


**Figure 2.** In this and all subsequent figures, the velocity, differential stress and strain rates at individual mesh points on the finite difference grid, when displayed, are at spacings of  $2L$  (that is: at every second mesh point in  $x$  and  $y$  for a  $32 \times 32$  grid and at every fourth point for a  $64 \times 64$  grid). Contours are drawn by a standard contouring routine that uses values from all the mesh points. This figure illustrates the velocity, strain rate and differential stress fields for a Newtonian fluid subject to the boundary conditions shown in Fig. 1 and discussed in the text, with  $Ar = 0$ . (a) Isotropic strain rate field (contours of the instantaneous rate of thickening or thinning:  $-(\dot{\epsilon}_{xx} + \dot{\epsilon}_{yy})$ ) for the flow field. The contours are from  $-1 \times 10^{-15} \text{ s}^{-1}$  (extension) in steps of  $2 \times 10^{-16} \text{ s}^{-1}$  to  $1.4 \times 10^{-15} \text{ s}^{-1}$ . Addition and subtraction signs mark locations of the maximum and minimum of the isotropic strain rate, and the zero contour is labelled. (b) Directions and magnitudes of the principal horizontal deviatoric stresses produced by the flow, the bar by the side of the figure shows the size of the symbol for the maximum stress. When  $Ar$  is zero, the absolute values of the stresses are arbitrary (see text) and this figure shows the variation of the relative magnitudes with distance from the influx boundary. The origins for the symbols lie on the mesh points; thick lines indicate negative stress (compression) and the thin lines indicate positive stress (tension). (c) Directions and magnitudes of the principal shear strain rates for the flow, the bar by the side of the figure shows the size of the symbol for the maximum strain rate ( $1.15 \times 10^{-15} \text{ s}^{-1}$ ). The centres of the symbols lie on the mesh points; thick lines correspond to dextral shear and the thin lines to sinistral shear. (d) Velocity vectors for the flow at individual mesh points; the origins for the vectors being at those points. The maximum velocity, shown by the bar at the side of the figure, is  $5 \text{ cm yr}^{-1}$ .

There are several features common to all the solutions shown. First, the flow (as indicated by the velocity vectors in Figs 2d, 3d and 4d) diverges from the influx portion of the southern boundary but, over most of the south-western portion of the box, it is still at a shallow angle to the  $y$ -axis; consequently the magnitude of  $u_y$  decreases laterally to follow closely the velocity boundary condition on the  $x$ -axis. This flow gives three distinct regions within the box which may be seen from the plots of isotropic strain rate (Figs 2a, 3a and 4a) and shear strain rate (Figs 2c, 3c and 4c). First, in the south-western corner of the box immediately in front of the influx boundary, is a region of intense compressive strain while there is a more

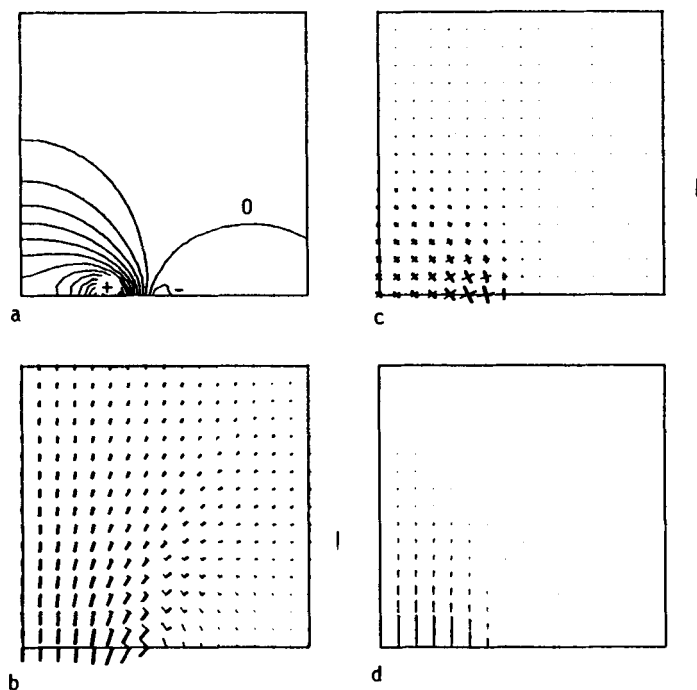


**Figure 3.** As for Fig. 2, except that the solutions are for a non-Newtonian power law fluid with  $n = 3$  and  $Ar = 0$ . (a) The strain rate contours are  $-2 \times 10^{-16}$  ( $2 \times 10^{-16}$ )  $2.8 \times 10^{-15} \text{ s}^{-1}$ . (c) The maximum principal shear strain rate is  $1.7 \times 10^{-15} \text{ s}^{-1}$ .

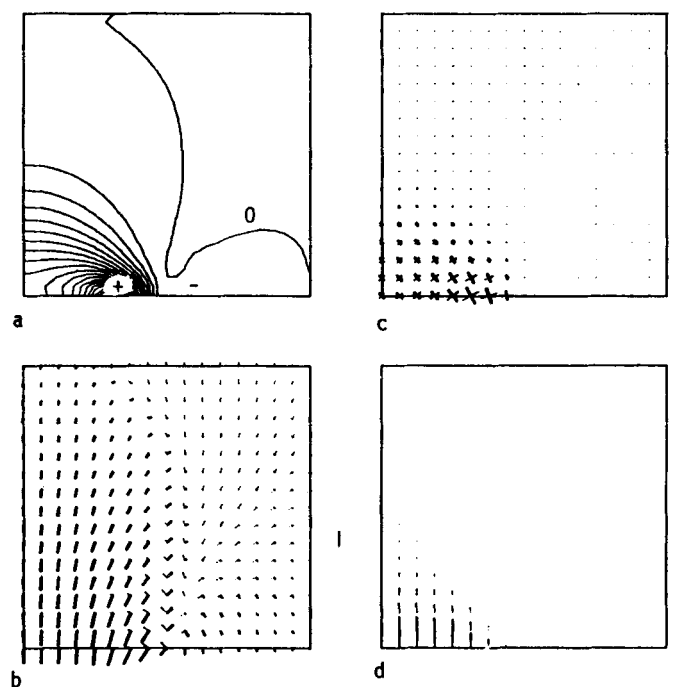


**Figure 4.** As Fig. 3, except that  $n$  is 5 and  $Ar$  zero. (a) The strain rate contours are  $0$  ( $2 \times 10^{-16}$ )  $3.6 \times 10^{-15} \text{ s}^{-1}$ . (c) The maximum principal shear strain rate is  $2.2 \times 10^{-15} \text{ s}^{-1}$ .

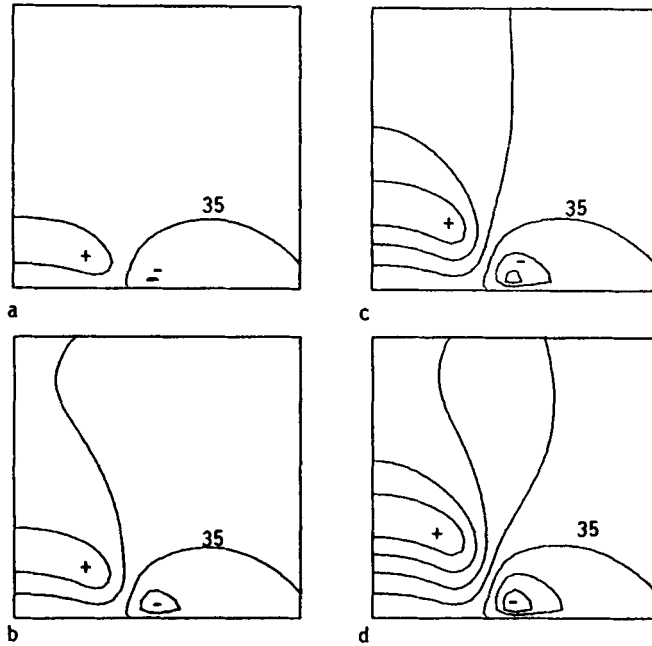


**Figure 5.** Plots of the crustal thickness as a function of time for the flow field of Fig. 2. Contours are at intervals of 5 km thickness; the addition and subtraction signs give the positions of maxima and minima; the initial crustal thickness, and the thickness of crust entering over the influx boundary, is 35 km. The 35 km contour is labelled. (a) Time is 7.9 Myr ( $tu_0$  400 km =  $4L$ ) contours are from 30 km in steps of 5 km to 40 km. (b) Time is 15.8 Myr ( $tu_0$  800 km =  $8L$ ) contours are 30 (5) 45 km. (c) Time is 23.7 Myr ( $tu_0$  1200 km =  $12L$ ) contours are 25 (5) 50 km. (d) Time is 31.2 Myr ( $tu_0$  1600 km =  $16L$ ) contours are 25 (5) 55 km.

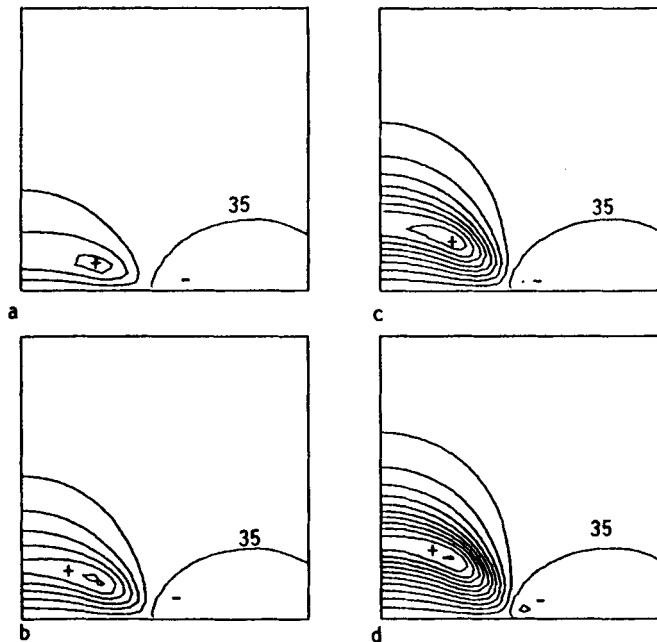


**Figure 6.** Plots of crustal thickness as a function of time for the flow field of Fig. 3. As Fig. 5. (a) Time is 7.9 Myr; contours are 35 (5) 50 km. (b) Time is 15.8 Myr; contours are 35 (5) 65 km. (c) Time is 23.6 Myr; contours are 30 (5) 75 km. (d) Time is 31.2 Myr; contours are 30 (5) 90 km.

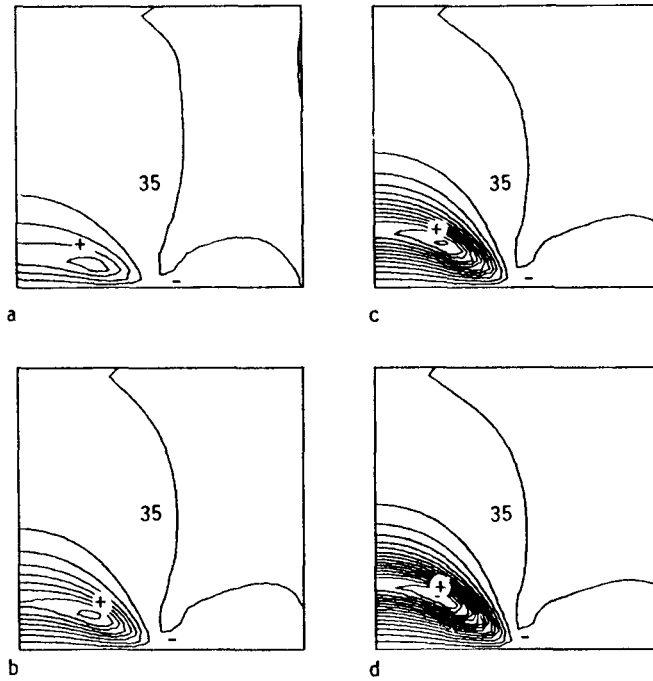


**Figure 7.** Plots of crustal thickness as a function of time for the flow field in Fig. 4. As Fig. 5. (a) Time is 7.8 Myr; contours are 35 (5) 55 km. (b) Time is 15.6 Myr; contours are 35 (5) 75 km. (c) Time is 23.4 Myr; contours are 35 (5) 95 km. (d) Time is 31.2 Myr; contours are 35 (5) 115 km.

diffuse region of extensional strain in the south-eastern corner. These two regions are separated by a zone of shearing associated with the transition from influx to zero motion on the southern boundary.

The origin of the extensional region can most readily be seen from the velocity field for  $n = 1$  (Fig. 2d), where there is an induced northward flow to the east of the influx boundary, which results in the tension near the fixed boundary to the south.

Although the flows discussed above have steady state velocity fields, they result in crustal thickness distributions which are time dependent (Figs 5, 6 and 7). Again, the flows for different values of  $n$  have several characteristics in common. The principal one is that, although the area of greatest rate of crustal thickening does not move (Figs 2a, 3a, 4a) the area of greatest crustal thickness is advected into the box and the maximum crustal thickness continues to increase, although more slowly as the region of greatest crustal thickness moves away from the inflow boundary.

The region of extension is associated with the rigid portion of the southern boundary and so does not move, and the total crustal thinning is very much less than the thickening in the compressive region of the flow.

We now consider those aspects of the flow field which are influenced by changing the value of  $n$  in the power law rheology. In the absence of pressure terms from crustal thickness variations, equation (16) takes the familiar form of the Euler equations for momentum conservation.

$$\frac{\partial}{\partial x_j} \left[ \eta_{\text{eff}} \left( \frac{\partial u_i}{\partial x_j} + \frac{\partial u_j}{\partial x_i} \right) \right] = 0 \quad (22)$$

where the effective viscosity,  $\eta_{\text{eff}}$ , is defined as

$$\eta_{\text{eff}} = B\dot{\epsilon}^{(1/n-1)} \quad (23)$$

(cf. equation 7). When the flow is Newtonian, the effective viscosity is constant, but in the cases where  $n$  is greater than unity the stress gradients have a contribution from the term in  $\partial\eta_{\text{eff}}/\partial x_j$ ; equation (11) may be written:

$$\frac{\partial \bar{p}}{\partial x_i} = \eta_{\text{eff}} \frac{\partial \dot{\epsilon}_{ij}}{\partial x_j} + \dot{\epsilon}_{ij} \frac{\partial \eta_{\text{eff}}}{\partial x_j}. \quad (24)$$

The second term on the rhs in equation (24) is equivalent to the second term on the rhs of equation (16), and is zero when  $n = 0$ . In general the magnitude and sign of this term depend on the details of the flow, but its effect is to concentrate the flow into the regions of highest stress, that is of lowest viscosity. This property is usually referred to as 'shear thinning'. As the scale of the flow in the  $x$ -direction is fixed in the present case, this concentration takes the form of diminishing the northward extent of the region of most intense deformation. Figs 2(a,c), 3(a,c), and 4(a,c) show that the maximum values of the isotropic and shear strain rates increase from 1.4 and  $1.15 \times 10^{-15} \text{ s}^{-1}$ , respectively for  $n = 1$  to 2.8 and  $1.5 \times 10^{-15} \text{ s}^{-1}$  for  $n = 3$  and to 3.6 and  $2.25 \times 10^{-15} \text{ s}^{-1}$  for  $n = 5$ . This effect can be seen in the plots of the velocity vectors (Figs 2d, 3d and 4d) and in the plots of  $u_y$  along the  $y$ -axis (Fig. 8a). Fig. 8(a) shows that the most pronounced changes come between  $n = 1$  and 3, although increasing  $n$  to 5 and 8 does further steepen the fall off of  $u_y$  with distance from the influx boundary.

In a similar manner, the concentration of the flow into the region around the influx boundary also reduces the magnitude of  $u_x$  (Figs 2d, 3d, 4d and 8b) as eastward motion away from the influx boundary is inhibited by the higher effective viscosity in the region of low strain rate. This is shown in the plots of  $u_x$  along the SW–NE diagonal (Fig. 8b); note that in the Newtonian case  $u_x$  is always positive near the influx boundary – in line with a general divergence of the flow from the source of material, but in the non-Newtonian cases the stress gradients discussed above produce small negative values of  $u_x$  in this region.

The changes in flow resulting from increasing  $n$  have a marked effect on the time development of the crustal thickness; the concentration of strain in front of the inflow boundary as  $n$  increases means that the crust reaches greater thicknesses there but the area of greatest thickness moves less far into the box because of the corresponding reduction of  $u_y$  (Fig. 8a).

A convenient measure of the width of the zone of crustal thickening is given by the intersection of the contour

$$s = (s_{\text{max}} + 35 \text{ km})/2 \quad (25)$$

with the  $y$ -axis. Comparing the width of this cut at, for example, 24 Myr shows that it changes from 1700 km wide for  $n = 1$  to 750 and 550 km for  $n = 3$  and 5 respectively; correspondingly, the maximum crustal thickness after 24 Myr increases from 50 km for  $n = 1$  to 75 and 95 km for  $n = 3$  and 5.

### 3.5 MODELS WITH $n = 3$ AND ARGAND NUMBER GREATER THAN ZERO

In this set of experiments, the velocity boundary conditions of Fig. 1 were used with the initial condition that the crust be 35 km thick everywhere in the box, but now the condition on the crustal thickness on the  $x$ -axis is that it has zero gradient normal to the boundary. This condition was used because for  $Ar > 3$ , a fixed crustal thickness at the influx boundary

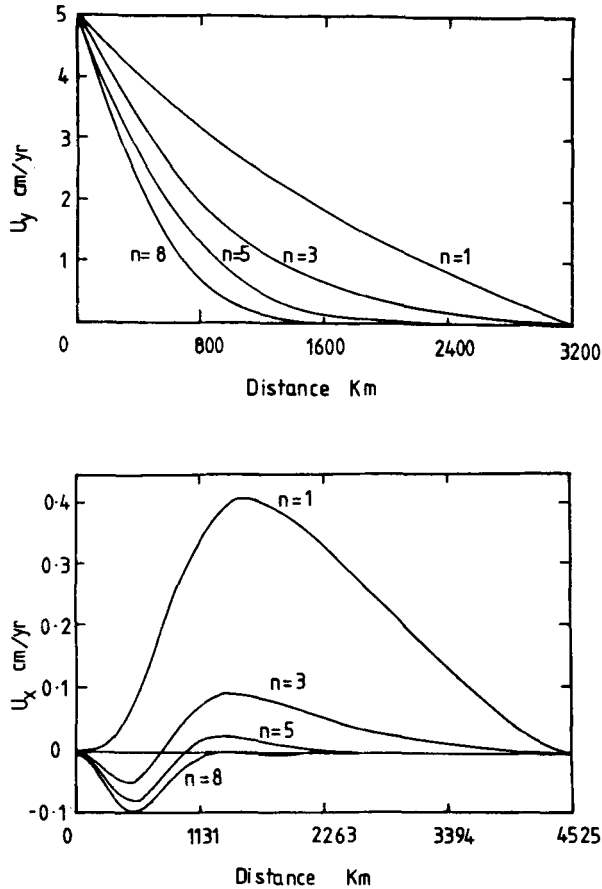


**Figure 8.** (a) Plots of  $u_y$  (northward velocity) with distance from the  $x$ -axis (south edge of box) along the  $y$ -axis for the boundary conditions illustrated in Fig. 1. The curves are for a Newtonian fluid ( $n = 1$ ; see Fig. 2a) and for power law fluids with  $n = 3$  (Fig. 3a),  $n = 5$  (Fig. 4a) and  $n = 8$  (not otherwise illustrated). (b) Plots of  $u_x$  (eastward velocity) with distance from the origin along the south-west–north-east diagonal of the box for the boundary conditions illustrated in Fig. 1. The curves are as for Fig. 8(a).

leads to very large gradients of crustal thickness near the boundary, which produce numerical instabilities. Figs 9–13 display the influence of increasing Argand number (decreasing effective viscosity) for  $n = 3$  in the type of flow discussed in the previous subsection.

We consider first the case where  $n = 3$  and  $Ar = 1$  (Figs 9 and 13a, b, c); because of the boundary condition on the  $x$ -axis, the area of thickest crust is now fixed on the inflow boundary, but the crustal thickness develops in a similar manner to that of Fig. 6 with an area of crustal thinning near the rest of the southern boundary (Fig. 9a, c, e and g). (The maximum crustal thickness is greater than in the case illustrated in Fig. 6 because the boundary condition requires more crustal material to enter the box as the crustal thickness builds up.)

The principal difference lies in the behaviour of the isotropic strain rate (Fig. 9b, d, f and h); Fig. 9(b) resembles the isotropic strain rate plot for the case when  $Ar$  is 0 (Fig. 3a) but as the crustal thickness in front of the inflow boundary increases, the forces arising from

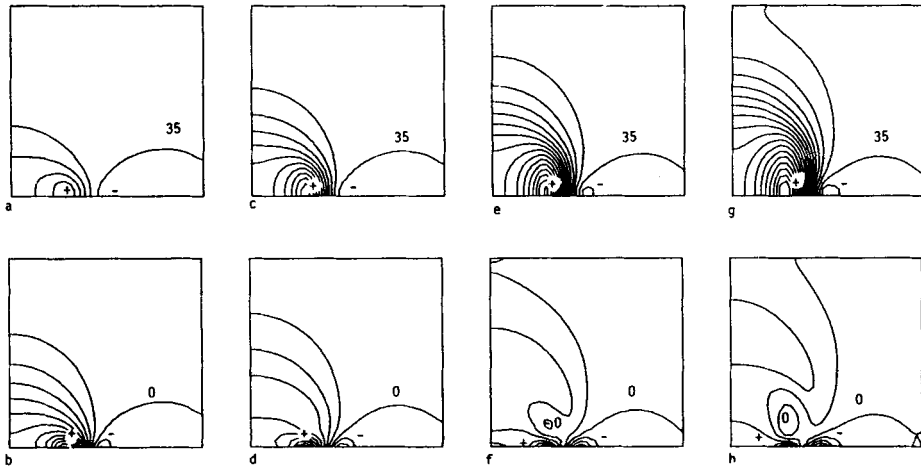


**Figure 9.** Contours of crustal thickness and isotropic strain rate for the boundary conditions of Fig. 1 with  $n = 3$  and  $Ar = 1$ ; initial crustal thickness everywhere is 35 km and the crustal thickness gradients are zero normal to each boundary. The crustal thickness is contoured at 5 km intervals and the strain rate at intervals of  $2 \times 10^{-16} \text{ s}^{-1}$ . (a) Time is 7.87 Myr: crustal thickness contours are from 35 km in steps of 5 km to 55 km. (b) Time is 7.87 Myr: isotropic strain rate contours are from  $-2 \times 10^{-16} \text{ s}^{-1}$  in steps of  $2 \times 10^{-16} \text{ s}^{-1}$  to  $2.4 \times 10^{-15} \text{ s}^{-1}$ . (c) Time is 15.8 Myr: crustal thickness 35 (5) 85 km. (d) Time is 15.8 Myr: isotropic strain rate  $-4 \times 10^{-16}$  ( $2 \times 10^{-16}$ )  $1.8 \times 10^{-15} \text{ s}^{-1}$ . (e) Time is 23.6 Myr: crustal thickness 30 (5) 110 km. (f) Time is 23.6 Myr: isotropic strain rate  $-6 \times 10^{-16}$  ( $2 \times 10^{-16}$ )  $1.0 \times 10^{-15} \text{ s}^{-1}$ . (g) Time is 31.5 Myr: crustal thickness 30 (5) 120 km. (h) Time is 31.5 Myr: isotropic strain rate  $-8 \times 10^{-16}$  ( $2 \times 10^{-16}$ )  $8 \times 10^{-16} \text{ s}^{-1}$ .

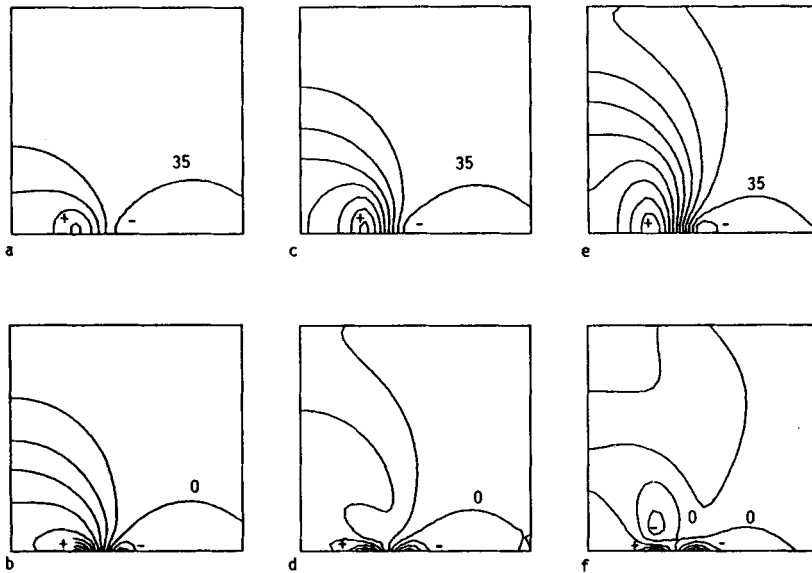


**Figure 10.** As Fig. 9, with  $n = 3$  and  $Ar = 3$ . (a) Time is 7.90 Myr: crustal thickness 35 (5) 55 km. (b) Time is 7.90 Myr: isotropic strain rate  $-4 \times 10^{-16}$  ( $2 \times 10^{-16}$ )  $1.8 \times 10^{-15} \text{ s}^{-1}$ . (c) Time is 15.8 Myr: crustal thickness 35 (5) 70 km. (d) Time is 15.8 Myr: isotropic strain rate  $-6 \times 10^{-16}$  ( $2 \times 10^{-16}$ )  $1.0 \times 10^{-15} \text{ s}^{-1}$ . (e) Time is 31.6 Myr: crustal thickness 30 (5) 80 km. (f) Time is 31.6 Myr: isotropic strain rate  $-6 \times 10^{-16}$  ( $2 \times 10^{-16}$ )  $6 \times 10^{-16} \text{ s}^{-1}$ .

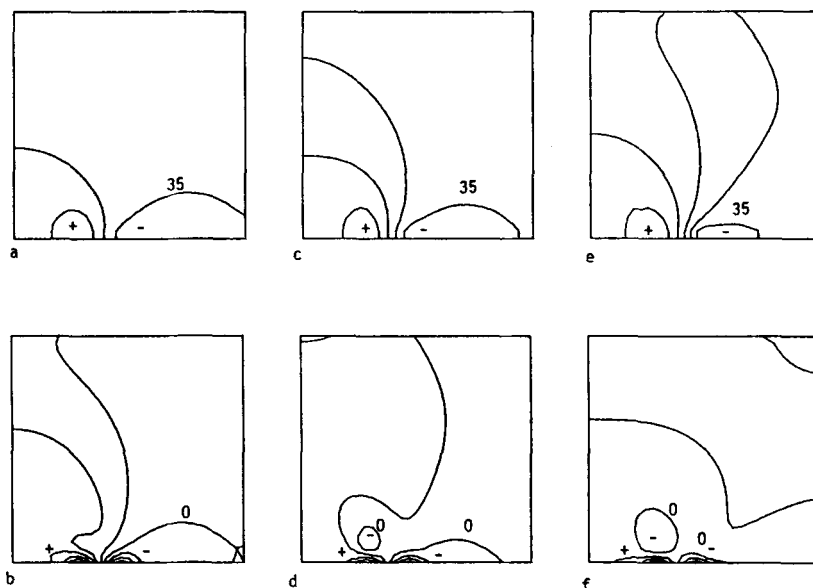


**Figure 11.** As Fig. 9, with  $n = 3$  and  $Ar = 10$ . (a) Time is 7.92 Myr: crustal thickness 35 (5) 45 km. (b) Time is 7.92 Myr: isotropic strain rate  $-6 \times 10^{-16}$  ( $2 \times 10^{-16}$ )  $1.2 \times 10^{-15} \text{ s}^{-1}$ . (c) Time is 15.8 Myr: crustal thickness 35 (5) 50 km. (d) Time is 15.8 Myr: isotropic strain rate  $-6 \times 10^{-16}$  ( $2 \times 10^{-16}$ )  $6 \times 10^{-16} \text{ s}^{-1}$ . (e) Time is 31.3 Myr: crustal thickness 35 (5) 55 km. (f) Time is 31.3 Myr: isotropic strain rate  $-4 \times 10^{-16}$  ( $2 \times 10^{-16}$ )  $6 \times 10^{-16} \text{ s}^{-1}$ .

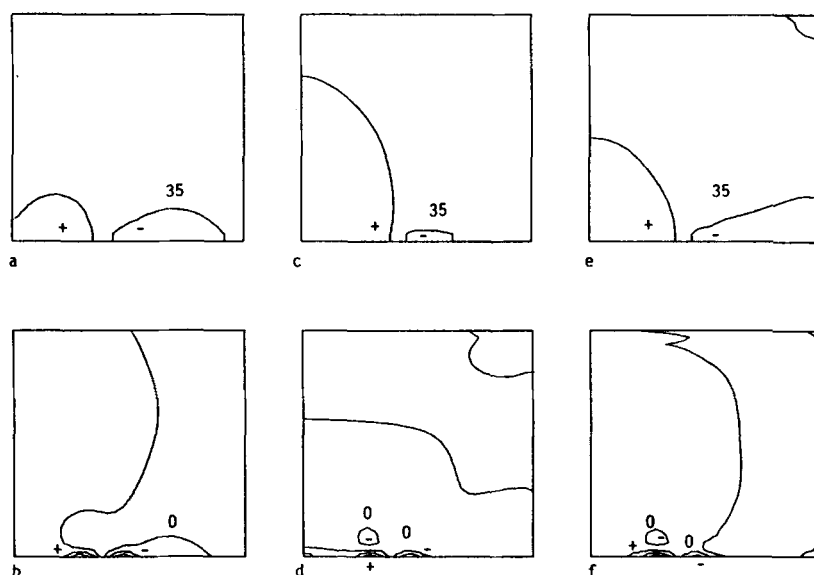


**Figure 12.** As Fig. 9, with  $n = 3$  and  $Ar = 30$ . (a) Time is 7.86 Myr: crustal thickness 35 (5) 40 km. (b) Time is 7.86 Myr: isotropic strain rate  $-4 \times 10^{-16}$  ( $2 \times 10^{-16}$ )  $6 \times 10^{-16} \text{ s}^{-1}$ . (c) Time is 15.6 Myr: crustal thickness 35 (5) 40 km. (d) Time is 15.6 Myr: isotropic strain rate  $-2 \times 10^{-16}$  ( $2 \times 10^{-16}$ )  $6 \times 10^{-16} \text{ s}^{-1}$ . (e) Time is 31.0 Myr: crustal thickness 35 (5) 40 km. (f) Time is 31.0 Myr: isotropic strain rate  $-2 \times 10^{-16}$  ( $2 \times 10^{-16}$ )  $6 \times 10^{-16} \text{ s}^{-1}$ .



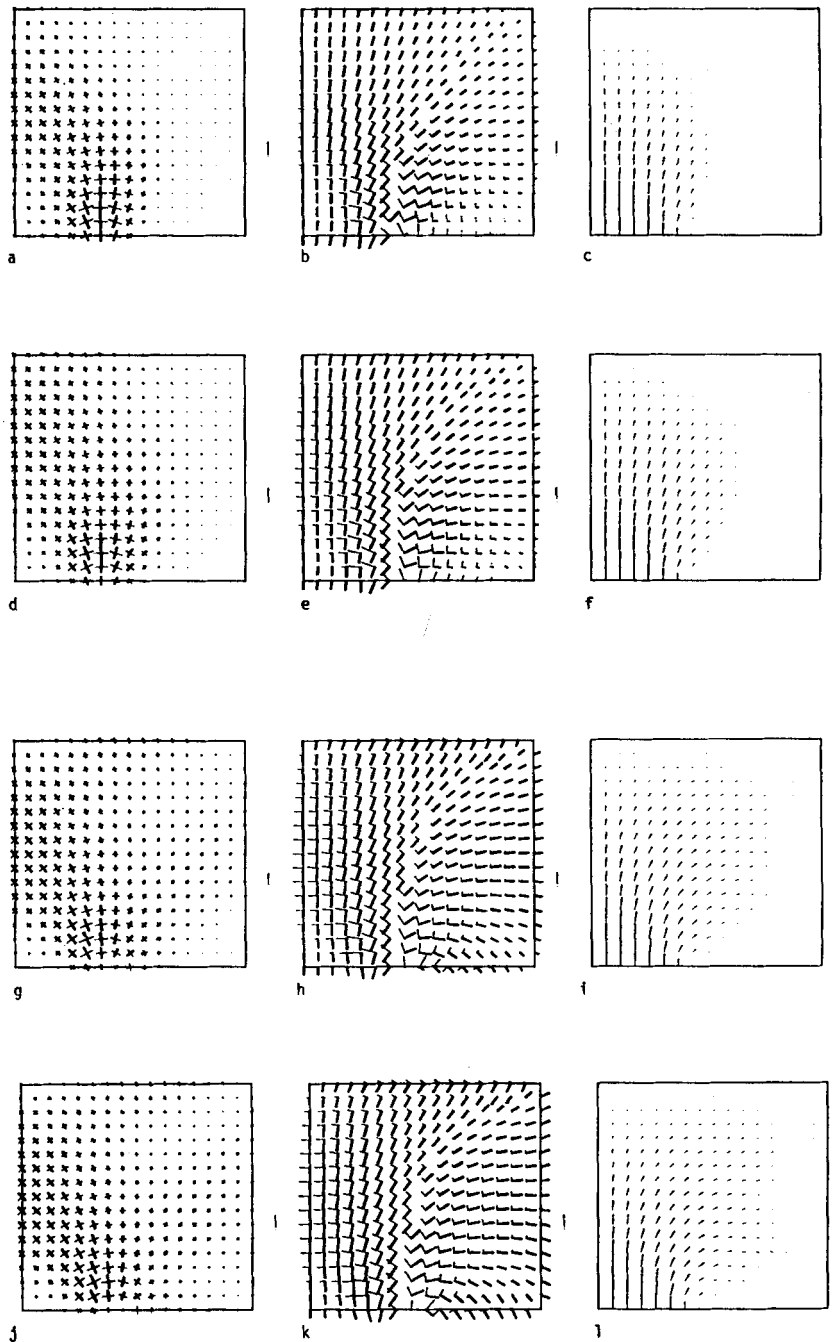


Figure 13. Plots of principal shear strain rates (Fig. 13a, d, g and j), principal deviatoric stresses (Fig. 13b, e, h and k), and of the velocity fields (Fig. 13c, f, i and l) for the numerical experiments with  $n = 3$  and different values of  $Ar$ . (a), (b) and (c):  $n = 3$  and  $Ar = 1$ ; plots at 31.5 Myr (see Fig. 9g and h). Maximum principal strain rates, principal deviatoric stresses and velocities, shown by bars at the sides of the figure, are  $8.8 \times 10^{-16} \text{ s}^{-1}$ , 1040 bar and  $5 \text{ cm yr}^{-1}$ . (d), (e) and (f);  $n = 3$  and  $Ar = 3$ ; plots for 31.6 Myr (see Fig. 10e and f):  $8.9 \times 10^{-16} \text{ s}^{-1}$ ; 340 bar and  $5 \text{ cm yr}^{-1}$ . (g), (h) and (i);  $n = 3$  and  $Ar = 10$ ; plots for 31.3 Myr (see Fig. 11e and f):  $9.3 \times 10^{-16} \text{ s}^{-1}$  100 bar and  $5 \text{ cm yr}^{-1}$ . (j), (k) and (l);  $n = 3$  and  $Ar = 30$ ; plots for 31.0 Myr (see Fig. 12e and f):  $9.5 \times 10^{-16} \text{ s}^{-1}$  31.8 bar and  $5 \text{ cm yr}^{-1}$ .

crustal thickness gradients start to affect the strain rate field. In the region where  $|s\nabla s|$  is largest an area of decreased rate of thickening develops, which finally becomes an area of net extension after 32 Myr (Fig. 9h). In addition, the region of appreciable crustal thickening extends only a distance comparable to the width of the influx boundary; in Fig. 9(b) the comparable region extends over more than half the width of the box.

These effects are more pronounced when the Argand number is 3; the lower effective viscosity of the medium allows the region of thickened crust to expand over a greater area of the box, and results in more extension on the rhs of the lower boundary than is seen when  $Ar$  is 1. Increasing  $Ar$  to 10 (Fig. 11) and 30 (Fig. 12) gives solutions in which the rates of extension of front of the inflow boundary and to the east of it become still greater.

There is also a striking change in the stress field as  $Ar$  is increased for constant  $n$ ; Fig. 13 shows the principal shear strain rates, principal stresses and velocity vectors for the models described with  $n = 3$  and  $Ar = 1, 3, 10$  and 30, at a time of 32 Myr (corresponding to Figs 9(g and h), 10(e and f), 11(e and f), 12(e and f)).

When  $Ar = 0$  (Fig. 3), the velocity vectors in front of the inflow boundary are predominantly in the  $y$ -direction (Fig. 3d). As  $Ar$  increases, the effective viscosity of the medium decreases and it is less able to support the stresses arising from crustal thickness contrasts. Even when  $Ar = 1$ , velocities comparable to  $u_0$  are found over much of the western half of the box (Fig. 13c), rather than being restricted to the region close to the inflow boundary (Fig. 3d), and there is now an appreciable component of eastward motion. The magnitudes of  $u_x$  increase with Argand number, until when  $Ar = 30$ , the strain associated with the injection of material over the inflow boundary is being accommodated to a large extent by motion of material eastwards in the eastern half of the box (Fig. 13). Shear strain rates comparable with those at the edge of the inflow boundary now occur over much of the western half of the box (Fig. 13a, d, g and j; compare Fig. 3b) and the principal stresses are close to purely compressive only immediately in front of the inflow boundary and near the eastern edge, where the rigid boundary stops the lateral flow (Fig. 13b, e, h and k; compare Fig. 3c).

#### 4 Discussion

The nature of the experiments and of the Earth preclude *direct* comparison of the fields illustrated in Section 3 with the patterns of motion at the Earth's surface in the region of a continental collision zone. In the first place, the upper crust deforms in a discontinuous manner by faulting and the formulation of Section 2 assumes a continuous viscous fluid throughout. Although faults are prominent in the surface geological record, they represent only the failure of the outermost, brittle layer of the lithosphere, and not that of the lithosphere as a whole. In addition, this brittle layer is likely to have an anisotropic fabric on a regional scale, owing to the alignment of faults and/or joints from previous tectonic events. Thus, the approach adopted in this paper will not predict explicitly the deformation of the outermost part of the lithosphere; we may expect, for example, thrust faulting in regions of shortening and normal faulting in regions of extension.

Secondly, continental lithosphere is heterogeneous on the large scale, consisting as it does of terrains of differing tectonic styles and ages; this heterogeneity must extend to lateral variation in the rheological properties of the lithosphere. An example of the effect of this heterogeneity may be the Tarim Depression which has remained essentially underformed throughout the Cenozoic (Molnar & Tapponnier 1978) and may be seen in Fig. 14 as a topographically low and seismically quiet region approximately  $8^\circ \times 4^\circ$  centred on  $38^\circ \text{N } 42^\circ \text{E}$ . Such heterogeneities may only be treated in an *ad hoc* fashion; their influence on the

geometry of deformation may well be significant if they are large enough (as has been suggested by Molnar & Tapponnier 1981) but we do not consider them further here.

Thirdly, the boundary conditions assumed for the numerical experiments are not necessarily those that apply during continental collision – and certainly the geometry does not correspond exactly to that of any real collision zone.

However, the purpose of this paper is *not* to model in detail a specific orogen but rather, by carrying out numerical experiments on the behaviour of power law materials in geometrically simple configurations, to gain some understanding of the large-scale processes involved in continental deformation. Several conclusions may be drawn from this approach which are independent of the detailed geometry and which contribute to our understanding of these large-scale processes.

The most dramatic example of continental collision at present is the convergence of the Indian subcontinent and Asia, and it is natural to compare the results of the numerical experiments with what is known of this collision. As outlined above, we shall be concerned with large-scale phenomena – principally crustal thickening – which have affected Asia since the collision with India 30–40 Myr ago. We take no account of the complex Mesozoic collision events in the region which, though still apparent in the geological record, were probably eroded flat by the time the major collision occurred in the middle Tertiary.

Figs 2–13 illustrate the deformation of fluids with power law rheologies over a wide range of conditions – from Newtonian to a rheology with stress exponent of 5, and from effective viscosities so high that the forces arising from crustal thickness variations do not affect the flow to ones so low that the crustal variations dominate the flow. It is of interest to know what portions of these parameter ranges produce models having similarities with real continental convergence zones.

Fig. 14 shows the topographic height averaged over  $1^\circ \times 1^\circ$  regions (Lee 1966) smoothed with a Gaussian filter of width  $2^\circ \times 2^\circ$ , and the seismic activity over the interval 1961–79 for the Indian sub-continent and Asia. Using the crust and upper mantle densities of Table 1, and assuming isostatic equilibrium, topographic height may be converted into excess crustal thickness by multiplying by a factor of 9.4. A thickness of 35 km will be assumed for crust with its surface at sea-level; thus maximum crustal thickness in Fig. 14 is taken to be about 82 km in central Tibet. The crustal thicknesses estimated by this method agree well with the sparser crustal thickness data summarized by Soller, Roy & Brown (1981).

The zone of crustal thickening to the north of India is extensive, but it does not reach the northern edge of the Eurasian continent, though it does approach more closely the eastern seaboard of China. Similarly, the seismic evidence for deformation of the region is largely confined to an area that has lateral dimensions about one and a half times to twice the width of the apparently rigid indenter – India (Fig. 14). In trying to assess what ranges of rheological parameters are appropriate to the deformation of the continents, a reasonable starting point is to discard those numerical experiments giving solutions in which the rigid boundaries to the box are the major means of confining the deformation; these conditions may apply to other types of continental deformation, but they do not seem appropriate to the Indian–Asian collision.

Figs 2–12 show that the smallest lateral extent of deformation (whether judged by crustal thickness or by the isotropic and shear strain rate fields) occurs when the Argand number is zero. Even in this case, the solutions for the Newtonian fluid exhibit deformation and crustal thickening that extend to the rigid boundaries of the region (Figs 2, 5 and 8); this situation would only be changed if the width of the indenter were very much less than the width of the box. The maximum crustal thickness produced by the flow is about 55 km after 32 Myr; with the assumptions about density made above, the corresponding maximum

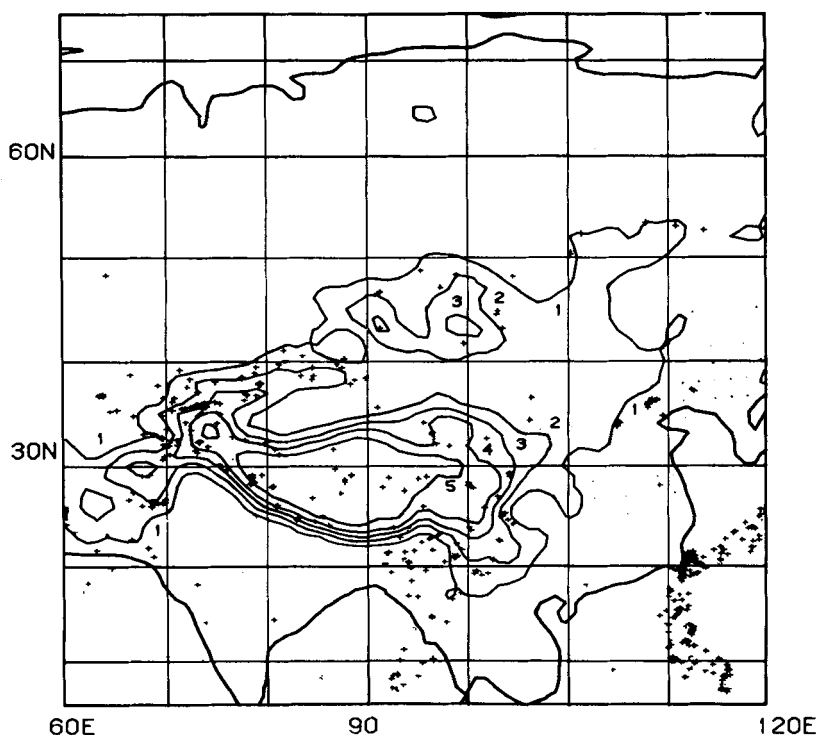


**Figure 14.** Average topographic elevation estimated over  $1^\circ \times 1^\circ$  elements (Lee 1966) and smoothed with a Gaussian filter of width  $2^\circ \times 2^\circ$ . The areas between  $10^\circ$  and  $60^\circ$  N and  $60^\circ$  and  $125^\circ$  E is contoured from 0 to 5 km in steps of 1 km. Superimposed on this are crosses which indicate the seismicity of the region around the Indian–Asian collision: each cross indicates an earthquake occurring between 1961 and 1977 and reported by at least 50 stations (data from NOAA Preliminary Determination of Epicentre Reports).

value in the Indian–Asian collision zone is 80 km. When a power law rheology is introduced the flow becomes much more restricted and the maximum crustal thicknesses after 32 Myr are 90 km ( $n = 3$ ) and 115 km ( $n = 5$ ) (Figs 6d and 7d).

Thus, if the continents have homogeneous rheological properties on the scale of hundreds to thousands of kilometres, it seems that some form of non-Newtonian rheology is required to explain the main features of the crustal thickness in Asia; assuming different boundary conditions will not change the conclusion that for a Newtonian fluid the deformation extends over a region with much larger lateral dimension than the width of the influx boundary, whereas for the power law materials the deformation is confined to a region of dimensions comparable with those of the indenter.

Even when the strength of the medium is low enough for the forces arising from crustal thickness variations to become important, it is possible to reproduce these conditions of crustal thickness with a medium obeying a power law rheology. The solutions discussed below are all for  $n = 3$ , but the same conclusions hold when  $n$  is 5, which is not illustrated.

Significant deformation does not occur on the distant edges of the box when the Argand number is equal to 1 or 3 (Figs 9, 10 and 13a–f), but for  $Ar = 10$  or 30 appreciable crustal thickening occurs at the edges of the boxes for all times (Figs 11, 12 and 13g–l). The

maximum crustal thickness attained is greater than 130 km for  $Ar = 1$  (more than 150 km with  $n = 5$ ), 80 km (95) for  $Ar = 3$ , 60 (65) for  $Ar = 10$  and 50 (50) for  $Ar = 30$ . While the latter two cases exhibit maximum crustal thicknesses that match those in collision zones such as the Alps the *form* of the crustal thickness variation (Figs 11 and 12) bears little resemblance to that in such areas.

The maximum deviatoric stresses produced by the flows at a time of 32 Myr (Fig. 13) are 1 kbar, 340, 100 and 32 bar for  $A = 1, 3, 10$  and 30 respectively. If the flow fields for  $Ar$  between 1 and 3 are representative of the deformation in the Himalayan–Tibet region, this implies that continental collision generates deviatoric stresses of half a kilobar to a kilobar within the lithosphere.

Although the dominant mode of deformation is compressional when the continental lithosphere is strong enough to maintain the kind of crustal thickness inferred for the Himalayas and Tibet ( $Ar$  is 1 or 3; Figs 9 and 10) it can be seen that after the crustal thickness exceeds about 100 km ( $Ar$  is 1) or 80 km ( $Ar$  is 3) a tensional regime develops in the area of maximum crustal thickness. The axes of least compressive stress are aligned perpendicular to the convergence direction and this shows an interesting agreement with the inferences of Cenozoic stretching in Tibet that have been made by Molnar & Tapponnier (1978) and Ni & York (1978). Another similarity between the numerical experiments and observations of the deformation in Tibet lies in the eastward movement of material to the north and east of the influx boundary when  $Ar$  is 3 or greater. Although this flow may be influenced to some extent by the geometry assumed for the boundary conditions it too has its origin in the outflow of material from the region of thickened crust (compare Figs 3d and 13f, i and l).

These two observations seem to be well established features of the Himalayan collision (Molnar & Tapponnier 1975, 1978; Ni & York 1978). The numerical experiments show that such a motion is the consequence of the flow of material away from a region of thickened crust in a lithosphere of finite viscosity. When the effective viscosity is infinite (zero Argand number, Figs 3 and 4) the strain of collision is accommodated almost entirely by compression parallel to the direction of convergence. The extension along strike when  $Ar$  is greater than zero is a direct consequence of the three-dimensional nature of the strain, which produces regions of elevated crust that spread outwards under their own weight and exert a lateral force on the surrounding continent. A mechanism like this was adumbrated by McKenzie (1972) in discussing the tectonics of the Mediterranean region.

The maximum strain rates in the experiments described above are around  $2$  or  $3 \times 10^{-15} \text{ s}^{-1}$  (Figs 2, 3 and 4) but the isotropic strain rates (thickening) drop below  $10^{-15} \text{ s}^{-1}$  once the limiting values of crustal thickness are approached at the influx boundary (Figs 9 and 10). These rates may be compared with the strain rates typical of the Himalayan collision if it is assumed that the present-day elevation of Tibet is largely the result of crustal thickening since India began to collide with Asia 30–40 Myr ago; this gives an average strain rate of around  $10^{-15} \text{ s}^{-1}$  if the initial crustal thickness has been approximately doubled.

The deviatoric stresses calculated for the models which have crustal thickness distributions broadly similar to that in Asia are between 300 and 2000 bar (Figs 9 and 13b and e); although the deviatoric stresses required to maintain the crustal thickness contrasts are not as large as this (see above) the velocities imposed by the boundary conditions generate large shear stresses near the edge of the influx boundary (Figs 9 and 13a, b, d and e).

This range of deviatoric stresses is comparable at its higher end to the static stresses estimated, for example, to be involved in the support of the outer rises, and at its lower end to the stresses regarded as typical for the dynamic stresses involved in plate motion and mantle convection. Near the lower end, the experiments in which stresses of around 300 bar are generated ( $Ar = 3$ ) produce crustal thickness variations compatible with those seen in

Asia and are not obviously at variance with other estimates for the dynamic state of stress in the Earth.

## 5 Conclusions

We have modelled the deformation of the continental lithosphere in terms of the behaviour of a thin viscous sheet of material obeying a power law rheology. For fixed geometry this behaviour is governed by the value of a dimensionless number, which we have called the Argand number, that is a measure of the tendency of the lithosphere to strain in response to the buoyancy forces that result from crustal thickness contrasts.

The broad zone of elevated continental crust to the north of the Indian–Asian collision suggests that the gross deformation of the continental lithosphere involves a considerable component of thickening to distances greater than 1000 km from the plate boundary. Thus, while instantaneous deformation may be most obvious at the surface as a finite number of major faults, it is possible that the time- and space-averaged deformation of Asia has approximated more closely to that of the homogeneous viscous sheet we have considered here.

In the numerical experiments described above, the large-scale deformation of the continental lithosphere over geological time-spans is assumed to be governed by the strength of the uppermost mantle and/or lower crust, which deforms as a power law material. The detailed rheology of this material is unknown because of the uncertainties in extrapolating relations obtained at laboratory strain rates to geological strain rates perhaps six orders of magnitude slower. Over a wide range of values for the rheological parameters the models predict that thickening of the continental crust occurs over areas of dimension at least as great as the width of the indenting continent. This is an important departure from the condition of plane strain assumed in the rigid-plastic indenter models of Molnar & Tapponnier (1975, 1978). Equally important is the result that, even when the lithosphere is able to support shear stresses of orders of a kilobar, the forces arising from crustal thickness contrasts play an important part in determining the flow field (Figs 9–12). The crustal thickness in front of the indenting continent is limited by the strength of the lithosphere; as the maximum crustal thickness is approached, stretching will begin to occur in the region of thickest crust.

Although there are uncertainties involved in the detailed comparison of numerical experiments with the real collision zones of the world (see Section 4), several conclusions can be drawn which depend more on the nature of the deforming material than they do on the geometry of the numerical experiments.

If the deformation of an approximately homogeneous viscous shell is to result in a distribution of crustal thickness qualitatively similar to that of the Himalayan collision, the requirement that crustal thickness contrasts of about 30 km should be maintained during collision implies that the continental lithosphere should be capable of sustaining shear stresses of about 300 bar at strain rates of about  $10^{-15} \text{ s}^{-1}$ . Similar stresses are also required if the deformation of the medium is not to be confined solely by the geometry of its margins. In addition, the medium should deform in a non-Newtonian fashion, for the deformation of a Newtonian fluid is far more diffuse than that of a power law material under these conditions (Figs 2, 3 and 4).

The stresses and strain rates in these numerical models, for boundary conditions appropriate to continental collision, are consistent with those inferred for present-day collision zones. Extrapolation of the laboratory determinations of the flow law of olivine to these strain rates would predict stresses in the range 300 bar–1 kbar for temperatures between 600 and 900°C (e.g. Ashby & Verrall 1978; Goetze 1978) – reasonable temperatures for the

uppermost mantle in a tectonically active region. It is likely that the strength of mantle materials is strongly dependent on temperature and with current estimates of the activation energy for creep (e.g. Goetze 1978; Ashby & Verrall 1978) a temperature change of 200°C at the top of the upper mantle would result in an order of magnitude change in the effective viscosity of the lithosphere. Consequently the type of regional deformation during continental collision may depend critically on the thermal regimes of the continents before collision (compare Figs 9 and 11 for example and see Molnar & Tapponnier 1981). We may speculate that the differing styles of Phanerozoic orogenic belts (for example the Alpine and Hercynian events in Europe (Zwart 1967) or the Alpine and Himalayan orogenies at present) are due to differing balances between the force available to drive continental collision and the strength of the continental lithosphere, rather than to any fundamental contrast in orogenic processes.

### Acknowledgments

PCE gratefully acknowledges support from an IBM Fellowship at the University of Cambridge where most of this work was carried out. This work is supported in part by National Science Foundation grant EAR-81-07659 and in part by an NERC grant. Peter Molnar provided several helpful discussions and the comments of an anonymous reviewer were useful. Department of Earth Sciences contribution no. 116.

### References

- Ashby, M. F. & Verrall, R. A., 1978. Micro mechanisms of flow and fracture, and their relevance to the rheology of the upper mantle, in *The Creep of Engineering Materials and of the Earth*, Royal Society, London.
- Buzbee, B. L., Golub, G. H. & Nielson, C. W., 1970. On direct methods for solving Poisson's equation, *Siam J. Numer. Anal.*, **7**, 627.
- Goetze, C., 1978. The mechanisms of creep in olivine, in *The Creep of Engineering Materials and of the Earth*, Royal Society, London.
- Lee, W. H. K., 1966. Analysis of the Earth's topography, in *Orbital Perturbations from Terrestrial Gravity Data*, Final Report, Contract AF (6d) – 4171, 213 pp., Institute of Geophysics and Planetary Physics, University of California, Los Angeles.
- McKenzie, D. P., 1972. Active tectonics of the Mediterranean system, *Geophys. J. R. astr. Soc.*, **30**, 109.
- McKenzie, D. P., 1976. Can plate tectonics describe continental deformation?, in *Structural History of the Mediterranean Basins*, eds Biju-Duval, B. & Montadert, L., Editions Technip, Paris.
- Molnar, P. & Tapponnier, P., 1975. Cenozoic tectonics of Asia: effects of a continental collision, *Science*, **189**, 419.
- Molnar, P. & Tapponnier, P., 1978. Active tectonics of Tibet, *J. geophys. Res.*, **83**, 5361.
- Molnar, P. & Tapponnier, P., 1981. A possible dependence of the tectonic strength on the age of the crust in Asia, *Earth planet. Sci. Lett.*, **52**, 107–114.
- Ni, J. & York, J. E., 1978. Late Cenozoic tectonics of the Tibetan Plateau, *J. geophys. Res.*, **83**, 5377.
- Richter, F. M. & McKenzie, D. P., 1978. Simple plate models of mantle convection, *J. Geophys.*, **44**, 441.
- Soller, D. R., Roy, R. D. & Brown, R. D., 1981. *A Global Crustal Thickness Map*, Phoenix Corporation, McClean, Virginia, 51 pp.
- Sweet, R. A., 1974. A generalized cyclic reduction algorithm, *Siam J. Numer. Anal.*, **11**, 506.
- Tapponnier, P. & Molnar, P., 1976. Slip-line field theory and large-scale continental tectonics, *Nature*, **264**, 319.
- Tapponnier, P. & Molnar, P., 1977. Active faulting and tectonics in China, *J. geophys. Res.*, **82**, 2905.
- Tullis, J. A., 1979. High temperature deformation of minerals, *Rev. Geophys. Space Phys.*, **17**, 1137.
- Zwart, H. J., 1967. The quality of orogenic belts, *Geologie Mijnb.*, **46**, 283–309.

### Appendix A: an average rheology for continental lithosphere

The deformation of a thin sheet of material, as discussed in this paper, will depend on the rheological properties of its strongest part. Laboratory determinations of the properties of crustal rocks are too scant, at present, to determine whether the lower crust or the upper mantle is likely to be the more competent in the continental lithosphere, indeed the balance may change from place to place within the continent depending on the abundances of the stronger minerals such as pyroxenes and feldspars (which at present have poorly determined rheologies) in the lower crust.

We shall assume that the strongest part of the continental lithosphere obeys a power law relation with an exponential dependence on absolute temperature (equation 1, Section 2). The result below is independent of whether this section is in the crust or mantle, and it will also hold if more than one section of the lithosphere, each with different activation energies for creep, contributes significantly to its strength. The conclusions will not hold if  $n$  is a function of position or temperature within the zone which controls the deformation of the lithosphere as a whole. Note that the significant element in this rheology is its 'shear thinning' property — that is, its effective viscosity decreases with increasing deviatoric stress. This has the effect of concentrating flow into the regions of highest stress; we might expect qualitatively similar results to those obtained in this paper for other shear thinning rheologies, but for the reasons outlined above we have chosen a power law rheology as a simple approximation to our present-day understanding of the rheology of rocks in steady state flow.

We have assumed (Section 2) that vertical gradients of horizontal velocity are negligible; consider a section of continental lithosphere undergoing shortening in the  $x$ -direction, with no strain in the  $y$ -direction. Then, in the notation of Section 2:

$$\begin{aligned}\dot{\epsilon}_{yy} = \dot{\epsilon}_{xy} = \dot{\epsilon}_{xz} = \dot{\epsilon}_{yz} &= 0 \\ \dot{\epsilon}_{xx} &= -\dot{\epsilon}_{zz}\end{aligned}\quad (\text{A1})$$

and similarly for  $\tau$ , thus

$$T = \sqrt{2} |\tau_{xx}| \text{ and } \dot{E} = \sqrt{2} |\dot{\epsilon}_{xx}|.$$

Equation (1) may be written

$$\dot{\epsilon}_{ij} = T^{n-1} \tau_{ij} C \exp(-Q/R\theta), \quad (\text{A2})$$

for the conditions (A1) we have

$$\pm \tau_{xx} = \mp \tau_{zz} = |\dot{\epsilon}_{xx}|^{1/n} (\sqrt{2})^{1/n-1} C^{-1/n} \exp(Q/nR\theta). \quad (\text{A3})$$

The required parameter in determining the deformation field is the stress averaged vertically through the lithosphere, i.e.

$$\frac{1}{L} \int_0^L \tau_{xx} dz = B \dot{\epsilon}_{xx}^{1/n} \int_0^L \exp(Q/nR\theta) dz \quad \text{for } \tau_{xx} \text{ positive.} \quad (\text{A4})$$

If we assume that the stress involved in the long-term deformation of the upper crust is much less than that required to deform the uppermost mantle and/or lower crust (see above), then equation (A4) may be written:

$$\frac{1}{L} \int_0^L \tau_{xx} dz \approx \frac{B \dot{\epsilon}_{xx}^{1/n}}{\beta} \int_{\theta_m}^{\theta_L} \exp\left(\frac{Q}{nR\theta}\right) d\theta \quad (\text{A5})$$



where it is assumed that the temperature in the lithosphere is given by

$$\theta(z) = \theta_0 + \beta z \quad (\text{A6})$$

and  $\theta_m$  and  $\theta_L$  are the temperatures at the top of the strong layer and at the base of the lithosphere respectively. Hence the average stress throughout the deforming lithosphere is related to the average strain rate by a relation of the form

$$\tau_{xx} = B \dot{\epsilon}_{xx}^{1/n} \quad (\text{A7})$$

provided that  $n$  remains constant. The value of  $B$  in equation (A7) depends weakly on the geothermal gradient in the strong layer,  $\beta$ , and strongly on the temperature at the top of the strong layer  $\theta_m$ .

### Appendix B: numerical solution of the equations

The form of equation (16) makes it natural to take advantage of one of the efficient algorithms that are available for solving Poisson's equation. The routine used was written by R. A. Sweet (1974) and uses a generalization of the cyclic reduction method described by Buzbee, Golub & Nielson (1970) to solve the standard finite difference approximation to the equation

$$r \frac{\partial^2 g}{\partial x^2} + \frac{\partial^2 g}{\partial y^2} = f(x, y) \quad (\text{B1})$$

on a rectangular mesh of spacing  $\Delta x$  in  $x$  and  $\Delta y$  in  $y$ . In the form used here,  $r$  is 2 or  $\frac{1}{2}$  (see below). The derivatives in this equation and in equation (14) are approximated by their standard space-centred finite difference forms, e.g.

$$\partial g / \partial x \approx \delta_x g = (h_{i+1,j} - h_{i-1,j}) / 2 \Delta x \quad (\text{B2})$$

$$\partial^2 g / \partial x^2 \approx \delta_x^2 g = (h_{i+1,j} - 2h_{ij} + h_{i-1,j}) / \Delta x^2 \quad (\text{B3})$$

$$\partial^2 g / \partial x \partial y \approx \delta_{xy}^2 g = (h_{i+1,j+1} + h_{i-1,j-1} - h_{i+1,j-1} - h_{i-1,j+1}) / 4 \Delta x \Delta y. \quad (\text{B4})$$

In this notation the finite differences ( $\delta_x$ ,  $\delta_x^2$ , etc.) are approximations to the derivatives ( $\partial/\partial x$ ,  $\partial^2/\partial x^2$ , etc.) and  $h_{ij}$  is an approximation to  $g(x_i, y_j)$ . The finite difference approximations to equation (16) are:

$$2\delta_x^2 u + \delta_y^2 u = -\delta_{xy}^2 v + 2(1-1/n) \dot{E}^{-1} (\dot{\epsilon}_{11} \delta_x \dot{E} + \dot{\epsilon}_{12} \delta_y \dot{E}) + Ar \dot{E}^{(1-1/n)} s \delta_x s \quad (\text{B5})$$

$$\frac{1}{2} \delta_x^2 v + \delta_y^2 v = \frac{1}{2} [-\delta_{xy}^2 u + 2(1-1/n) \dot{E}^{-1} (\dot{\epsilon}_{22} \delta_y \dot{E} + \dot{\epsilon}_{12} \delta_x \dot{E}) + Ar \dot{E}^{(1-1/n)} s \delta_y s]. \quad (\text{B6})$$

The requirement that the coefficient of  $\delta_y^2 g$  be unity (equation B1) is responsible for the forms of (B5) and (B6). In these equations  $u$  and  $v$  are approximations to the  $x$  and  $y$  components of  $\mathbf{u}$ ; they are calculated on a rectangular mesh, as is the value of the crustal thickness,  $s$ . Note that  $\dot{E}$  and the components of  $\dot{\epsilon}$  are derivatives of velocity and appear in equations (B5) and (B6) as difference approximations to these derivatives.

The equations are solved by an iterative procedure: initial guesses are made for  $u$  and  $v$  by setting the rhs of (B5) and (B6) to zero and using the Poisson-solving routine. These estimates

are used to construct new rhs for equations (B5) and (B6), and new solutions for  $u$  and  $v$  are obtained by combining the solutions given by the Poisson-solving routine  $u_p, v_p$  with the previous estimates:

$$u_{\text{new}} = \alpha u_p + (1 - \alpha) u_{\text{old}} \quad (\text{B7})$$

and new rhs are calculated. The process is iterated until the largest change in either velocity component is less than a desired fraction of the maximum velocity in the system:

$$|u - u_{\text{old}}|_{\text{max}} / |u_{\text{old}}|_{\text{max}} < \beta. \quad (\text{B8})$$

The solution is then time-stepped using a finite difference approximation to equation (18):

$$s_{ij}^{n+1} = s_{ij}^n - \frac{\Delta t}{\Delta x} [s_E u_E - s_W u_W] - \frac{\Delta t}{\Delta y} [s_N v_N - s_S v_S] \quad (\text{B9})$$

where

$$\begin{aligned} u_E &= (u_{i+1,j} + u_{ij})/2; & u_W &= (u_{i-1,j} + u_{ij})/2 \\ v_N &= (v_{i,j+1} + v_{i,j})/2; & v_S &= (v_{i,j-1} + v_{i,j})/2 \end{aligned} \quad (\text{B10})$$

and

$$\begin{aligned} s_E &= s_{ij} & u_E > 0; & & s_{i+1,j} & u_E < 0 \\ s_W &= s_{i-1,j} & u_W > 0; & & s_{i,j} & u_W < 0 \\ s_N &= s_{ij} & v_N > 0; & & s_{i,j+1} & v_N < 0 \\ s_S &= s_{i,j-1} & v_S > 0; & & s_{i,j} & v_S < 0. \end{aligned} \quad (\text{B11})$$

The superscripts  $n, n+1$  indicate successive time levels,  $\Delta x$  and  $\Delta y$  are grid spacing in the  $x$  and  $y$  directions and the size of the time-step  $\Delta t$  is chosen to satisfy the Courant-Friedrichs-Lewy stability criterion:

$$\Delta t / (|u_{ij}|_{\text{max}} + |v_{ij}|_{\text{max}}) \leq 1. \quad (\text{B12})$$

This 'upwind' differencing scheme was chosen in preference to the properly centred scheme because the latter scheme was prone to time level splitting — the development of disjoint solutions at alternate time levels. Upwind differencing avoids this at the expense of introducing a numerical diffusion; this scheme gives results that agree to within a few per cent with those obtained from a space- and time-centred approximation to equation (18) when the latter does not have time level splitting. The differences, as would be expected, take the form of a slight smoothing out of crustal thickness variations in the upwind scheme relative to the space and time centred scheme.

The routine for solving Poisson's equation was tested against exact solutions to the finite difference equation

$$\delta_x^2 g + \delta_y^2 g = f_{ij} \quad (\text{B13})$$

and was found to be accurate to better than one part in  $10^4$  for  $f_{ij}$  having components of wavelength 2 mesh spacings or more.

The iteration scheme described above is robust, and when the last two terms on the rhs of equation (16) are small compared to the first one,  $\alpha$  (equation B6) may generally be chosen as unity. If  $Ar$  in equation (16) is much less than one, or is zero, the velocity field is almost,

or completely, independent of time and the solution for the velocity field may be found from the initial guess in four iterations for  $n = 1$ ,  $Ar = 0$  and in 21 iterations for  $n = 3$ ,  $Ar = 0$ . These figures are for a value of  $10^{-3}$  for  $\beta$  in equation (B8); a further two and four iterations respectively are required for convergence to one part in  $10^4$ .

The efficiency of this scheme varies according to the type of solutions sought, and when the last two terms in equation (16) become large – particularly when  $Ar \geq 3$  and  $n \geq 3$  – values of  $\alpha$  as small as  $10^{-2}$ , and several hundred iterations, may be required to reach a solution, and the solutions may be strongly time-dependent for  $Ar \geq 1$ , requiring a lengthy computation for *each* time-step. Over-relaxation ( $\alpha > 1$ ) is not stable. A value of  $2.5 \times 10^{-3}$  was usually taken for the indicator of convergence in equation (B7); lower values did not significantly affect solutions.

For the geometries described in this paper, the solutions were obtained on a  $32 \times 32$  mesh; selected combinations of parameters were also run on a  $64 \times 64$  mesh to check that the solutions were adequately resolved. Fig. B1 shows the comparison between solutions obtained on  $32 \times 32$  and  $64 \times 64$  meshes for the combination  $n = 5$ ,  $Ar = 30$ ; there is good agreement between the isotropic strain rates (illustrated) and the shear strain rates; these, as they involve derivatives of the velocity field, are particularly sensitive to differences between the solutions. An indication of the extent to which the crustal thickness is affected by moving to a finer mesh may be seen by comparing the rms difference between the crustal thickness at time 21 Myr and that at time 0 – where it is a uniform 35 km. In the  $32 \times 32$  calculation this rms difference is 6.28 km and in the  $64 \times 64$  calculation it is 6.27 km; the difference is at the 0.2 per cent level.

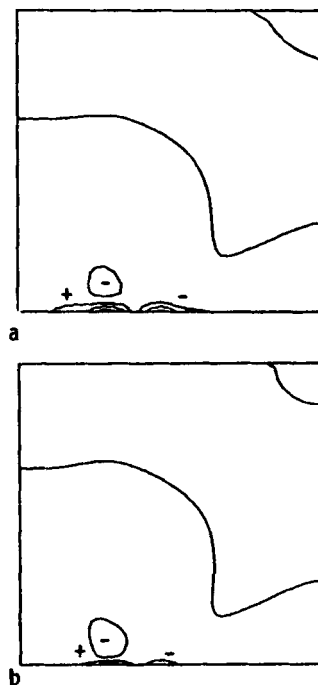


**Figure B1.** Contours of the isotropic strain rates for  $n = 5$ ,  $Ar = 30$  after 21 Myr. (a) Solutions calculated on  $32 \times 32$  mesh. Contours are  $-4 \times 10^{-16} \text{ s}^{-1}$  ( $2 \times 10^{-16}$ )  $6 \times 10^{-16} \text{ s}^{-1}$ . (b) Solutions calculated on  $64 \times 64$  mesh. Contours are  $-2 \times 10^{-16} \text{ s}^{-1}$  ( $2 \times 10^{-16}$ )  $4 \times 10^{-16} \text{ s}^{-1}$ .